

Calving seismicity from iceberg–sea surface interactions

T. C. Bartholomaus,^{1,2} C. F. Larsen,¹ S. O’Neel,^{2,3} and M. E. West^{1,2}

Received 11 June 2012; revised 27 September 2012; accepted 10 October 2012; published 22 December 2012.

[1] Iceberg calving is known to release substantial seismic energy, but little is known about the specific mechanisms that produce calving icequakes. At Yahtse Glacier, a tidewater glacier on the Gulf of Alaska, we draw upon a local network of seismometers and focus on 80 hours of concurrent, direct observation of the terminus to show that calving is the dominant source of seismicity. To elucidate seismogenic mechanisms, we synchronized video and seismograms to reveal that the majority of seismic energy is produced during iceberg interactions with the sea surface. Icequake peak amplitudes coincide with the emergence of high velocity jets of water and ice from the fjord after the complete submergence of falling icebergs below sea level. These icequakes have dominant frequencies between 1 and 3 Hz. Detachment of an iceberg from the terminus produces comparatively weak seismic waves at frequencies between 5 and 20 Hz. Our observations allow us to suggest that the most powerful sources of calving icequakes at Yahtse Glacier include iceberg–sea surface impact, deceleration under the influence of drag and buoyancy, and cavitation. Numerical simulations of seismogenesis during iceberg–sea surface interactions support our observational evidence. Our new understanding of iceberg–sea surface interactions allows us to reattribute the sources of calving seismicity identified in earlier studies and offer guidance for the future use of seismology in monitoring iceberg calving.

Citation: Bartholomaus, T. C., C. F. Larsen, S. O’Neel, and M. E. West (2012), Calving seismicity from iceberg–sea surface interactions, *J. Geophys. Res.*, *117*, F04029, doi:10.1029/2012JF002513.

1. Introduction

[2] Iceberg calving may take many forms, ranging from the slow rifting of tabular icebergs with decadal recurrence times [e.g., *Bassis et al.*, 2005], to the failure of relatively intact, kilometer-scale, full-glacier-thickness icebergs with week to month recurrence times [e.g., *Amundson et al.*, 2008; *Joughin et al.*, 2008], to the crumbling release of smaller seracs with minute to hour recurrence times [e.g., *O’Neel et al.*, 2003]. Individual calving events often include elements of each of these. For example, *Walter et al.* [2012] describe a sequence of calving events in which two full-glacier-thickness icebergs rotate out from the terminus accompanied by innumerable smaller serac failures over a period of 12 minutes.

[3] Across this continuum of events at glacier termini, iceberg calving is a source of seismic energy [e.g., *Qamar*, 1988; *O’Neel et al.*, 2007; *Amundson et al.*, 2008; *Joughin*

et al., 2008; *Tsai et al.*, 2008]. Previously reported seismic events have been recorded on networks that span a broad range of scales, from relatively small (earthquake magnitude 1–2) events recorded at kilometer-scales [*Qamar*, 1988; *O’Neel et al.*, 2007], up to magnitude 5 events recorded globally [*Ekström et al.*, 2003; *Tsai and Ekström*, 2007; *Nettles and Ekström*, 2010]. Calving seismicity is distinct from tectonic earthquakes in both their proposed sources and the appearance of their waveforms. Typically, these calving-generated seismic events lack clear *P*- and *S*-wave arrivals, have emergent onsets and, when observed at regional scales (<100 km) in both Alaska and Greenland, have maximum power spectral densities between 1 and 5 Hz [e.g., *Wolf and Davies*, 1986; *Qamar*, 1988; *Amundson et al.*, 2008; *O’Neel et al.*, 2010; *Walter et al.*, 2012]. However, despite widespread observation of calving seismicity, it remains unclear as to what part or parts of the iceberg calving process create these seismic signals.

[4] Various mechanisms related to iceberg calving have been proposed as sources for calving seismicity. For example, glacial earthquakes most frequently associated with outlets of the Greenland Ice Sheet (summarized by *Nettles and Ekström* [2010]) have been ascribed to the rotation of buoyantly unstable icebergs following detachment [*Tsai et al.*, 2008; *Amundson et al.*, 2010]. These icebergs scrape against the seafloor or the terminal cliff as they rotate, exerting a horizontally directed force. However, large, full thickness iceberg calving is absent at most glaciers in Alaska and Greenland [e.g., *Walter et al.*, 2010]. Even where full

¹Geophysical Institute, University of Alaska Fairbanks, Fairbanks, Alaska, USA.

²Department of Geology and Geophysics, University of Alaska Fairbanks, Fairbanks, Alaska, USA.

³Alaska Science Center, U.S. Geological Survey, Anchorage, Alaska, USA.

Corresponding author: T. C. Bartholomaus, Geophysical Institute, University of Alaska Fairbanks, 903 Koyukuk Dr., Fairbanks, AK 99775, USA. (tbartholomaus@gi.alaska.edu)

©2012. American Geophysical Union. All Rights Reserved.
0148-0227/12/2012JF002513

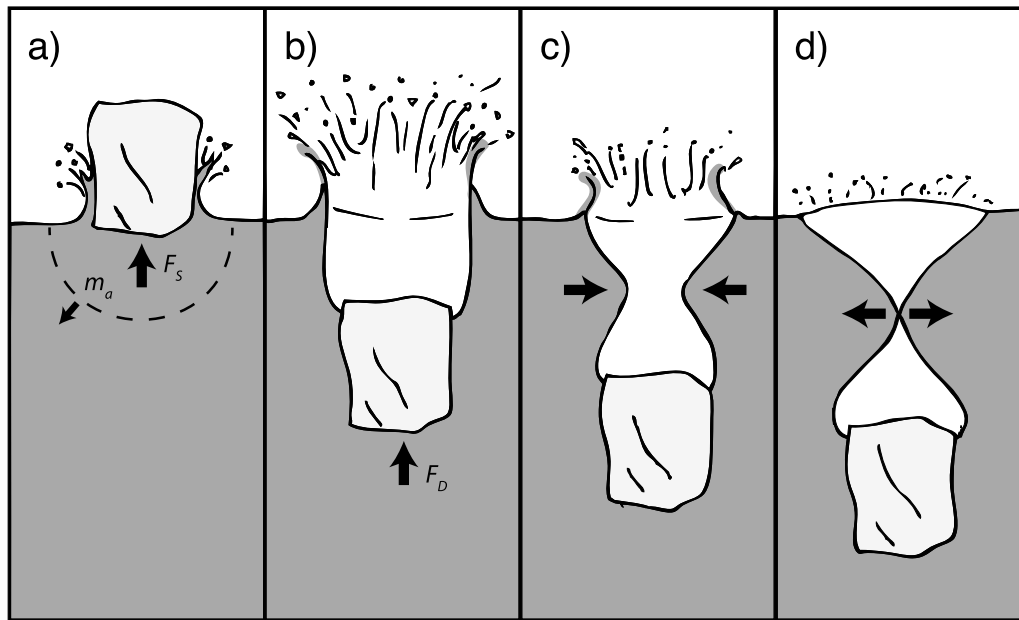


Figure 1. Cartoon representing four seismogenic mechanisms involving iceberg/fjord interaction: (a) slamming, i.e., momentum transfer to seawater, (b) iceberg deceleration, (c), cavity collapse, and (d) cavity pinch off. A Worthington jet forms immediately after Figure 1d. Arrows represent forces and accelerations. Illustration after *Gekle and Gordillo* [2010].

thickness calving occurs, not every calving event involves this rotation mechanism. Thus, other potential seismogenic mechanisms must be active. Mechanisms reported in existing literature include ice fracture [*Neave and Savage*, 1970; *Deichmann et al.*, 2000; *Walter et al.*, 2009; *West et al.*, 2010], pressure fluctuations in subglacial conduits [*St. Lawrence and Qamar*, 1979; *Winberry et al.*, 2009; *West et al.*, 2010; *Carmichael et al.*, 2012], resonating water-filled cracks and hydro-fracture [*O’Neel et al.*, 2007], basal slip [*Wiens et al.*, 2008; *Winberry et al.*, 2011], and grinding and fracturing within an ice mélange [*Amundson et al.*, 2010]. However, in many cases, no consensus exists on which mechanism or mechanisms are dominant.

[5] Iceberg interactions with the sea surface represent another suite of potential seismogenic mechanisms. *Qamar* [1988] demonstrated that the change in gravitational potential energy associated with a moderately sized calving event may easily generate seismic waves with energies comparable to the icequakes reported by *Wolf and Davies* [1986]. Icebergs that forcefully impact the water surface from above rapidly transfer momentum to the seawater, then more gradually continue to lose momentum through drag exerted against the surface of the iceberg. These momentum changes are associated with water accelerations that could be transmitted as compressional seismic waves. If an iceberg descends below the sea surface, then a submarine air cavity can form in the lee of the iceberg. The extremely high pressures developed during cavitation are known to be important in other geophysical disciplines [e.g., *Whipple et al.*, 2000; *Spray*, 1999] and the seismic signature of cavitation has been detected within volcanic magma conduits [e.g., *Chouet et al.*, 1997]. In the case of calving, cavitation may also be seismically detectable. High-speed, “Worthington” jets that emerge from the sea surface following complete

submergence of an iceberg are perhaps the most easily observed evidence of calving cavitation. Worthington jets occur when the walls of a collapsing cavity meet to fully enclose the cavity [*Gekle and Gordillo*, 2010]. From the pinch-off point, jets of water emerge with velocities far in excess of the initial crown splash velocity. These iceberg/fjord interactions are schematically illustrated in Figure 1. In this study, we explore the extent to which iceberg-sea surface interactions generate icequakes.

[6] Before seismicity can be quantitatively tied to iceberg volume, glaciologists and seismologists must first be able to identify what mechanisms are releasing the observed seismic energy. The source of seismic energy, generated either by ice fracture, ice crumbling along the terminal cliff, rotating icebergs scraping the ocean bottom, or through iceberg interactions with the sea surface has major implications for how calving seismicity can be used in future glaciological investigations. To address the question of icequake seismogenesis, we return to the terminus of Yachtse Glacier, where *O’Neel et al.* [2010] identified a dense cluster of icequake epicenters.

2. Setting

[7] Yachtse Glacier is an advancing, grounded, tidewater glacier and the largest of four glaciers that terminate in Icy Bay, Alaska (Figure 2). It is 63 km long with a surface area of 1018 km² and includes a broad, low-gradient upper basin between 900 and 1400 m elevation. This upper basin drains through an icefall (1% of glacier area) that falls from 700 m elevation to sea level over a distance of 5 km (this lowest reach is depicted in Figure 2). Laser altimetry of the glacier’s longitudinal profile and water depth soundings extrapolated from as close as 1.5 km from the terminus indicate that the glacier is approximately 170 m thick at its centerline, in water

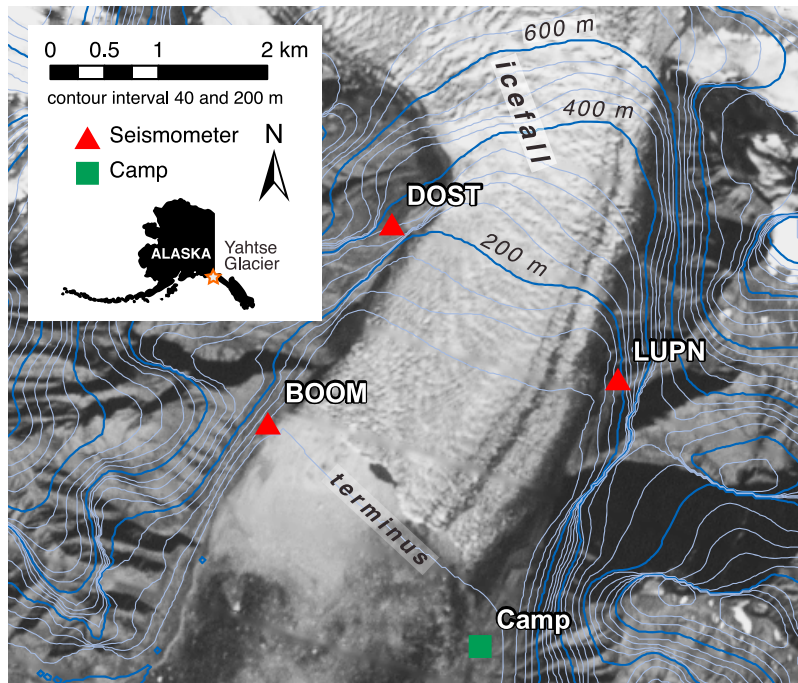


Figure 2. Map of lowest 5 km of 60 km-long Yahtse Glacier, including the icefall above the terminus. The locations of 3 out of 10 seismometers installed at the glacier margin are shown. Additional bedrock and in-ice seismometers, as well as on-ice GPS receivers, are off the map to the north, south, and west. Time-lapse cameras taking photographs of the terminus every 20 min between June 2009 and September 2011 were at the locations of BOOM, DOST, and Camp. Background image is from the panchromatic band of Landsat 7 on 12 Sept. 2010, approximately 5 days after the video used in this study was recorded. Topography is from 2000, Shuttle Radar Topography Mission.

approximately 110 m deep. Thus, the terminus is grounded, as its height is well above the level at which it would float.

[8] The terminus of Yahtse Glacier is composed of relatively fracture free seracs bounded by deep (>30 m), transverse crevasses and highly fractured interstitial ice. The terminus-parallel dimension of the seracs is greater than the terminus-perpendicular dimension—likely a result of the principal tensile stress being oriented with the glacier flow direction. In time-lapse photography looking across the direction of flow (introduced in the next section), ice motion within the last few hundred meters of the terminus sometimes appears to have a significant vertical component superimposed on its mean down-fjord motion. We interpret this vertical component as the glacier moving up and over a submarine terminal moraine.

[9] Yahtse and its three tidewater neighbors in Icy Bay had completely filled Icy Bay in the late 19th century, extending 40 km beyond its present terminus to the Gulf of Alaska [Porter, 1989; Barclay *et al.*, 2006]. At the conclusion of the Little Ice Age, the Icy Bay glaciers began retreating at an average rate of 400 m/yr. Simultaneous with this terminus retreat, the glacier above 700 m thinned insignificantly [Muskett *et al.*, 2008]. In approximately 1990, Yahtse Glacier concluded the retreat phase of the tidewater glacier cycle and began advancing [Meier and Post, 1987]; as of September 2011, the terminus of Yahtse Glacier is 2.0 km beyond this minimum position.

[10] Icy Bay is also a known center of icequake activity. The Alaska Earthquake Information Center, as part of its

long-term monitoring of earthquakes, has long recognized and cataloged seismicity associated with glacier activity as distinct from tectonic or volcanic sources (Alaska Earthquake Information Center, Monthly Earthquake Catalogs, 2012, available at http://www.aeic.alaska.edu/html_docs/monthly_reports.html). Many of these icequakes originate in the St. Elias Range, an approximately 80 km by 220 km glacierized region of south central and southeast Alaska, where Yahtse Glacier is located. In October 2006, 1016 icequakes were identified within the St. Elias range with a median local magnitude of 1.08 [O’Neel *et al.*, 2010]. Of these, 51% of epicenters located within 15 km of the terminus of Yahtse Glacier; typical location errors were on the order of 5–10 km. An additional 37% of the icequakes located within 15 km of the tidewater termini of nearby Guyot and Tyndall glaciers. O’Neel *et al.* [2010] attributed this concentration of icequakes to calving and suggested that icequake detection algorithms could be used as calving counters in regions with tidewater glaciers.

3. Methods

[11] Our analysis relies on three independent but complementary methods: seismic recordings, in-person observation of terminus calving events, and video recordings and time-lapse photography of the terminus. The data for this analysis were collected at Yahtse Glacier during 1–14 June and 7–8 September, 2010. These data represent a small portion of

a much larger and more diverse data set collected between June 2009 and September 2011.

3.1. Seismic Recordings

[12] During 2010, the seismic network at Yahtse Glacier consisted of sensors deployed on ice and on solid earth around the glacier. The seismic data discussed in this paper comes from the station closest to the glacier terminus, BOOM, installed on a ~ 30 m high ledge, 400 m from the western edge of the 2010 terminus of Yahtse Glacier (Figure 2). BOOM was one of ten broadband, 3-component seismometers installed on bedrock and in shallow sediment; the seismic signals recorded by the other stations are not markedly different than those from BOOM. The locations of three sensors are shown in Figure 2. Almost all of these sensors, including BOOM, were Guralp 3Ts, with a flat response between 120 s and 50 Hz. We converted the seismic data from raw counts to velocity but did not correct for instrument frequency response. Because of the flat response and no gain within the frequency range of interest, instrument response deconvolution was unnecessary. All data were recorded by Quanterra 330 digitizers and balers sampling at 200 Hz.

3.2. Observer Record

[13] During June 2010, focused observation of the Yahtse Glacier terminus was maintained for 81 hours over 13 days, in a manner similar to that used in *O'Neel et al.* [2007]. Observation was carried out from camp at the eastern edge of the terminus. The field of view included approximately 60% of the glacier's terminal cliff. Observers recorded every visible or audible event, with a descriptor for the style or type of event, a qualitative iceberg size, the event time, the event duration, and the event location on the terminus. Equally important, the timing of quiet periods without events was also recorded. Thus, variations in the rate of iceberg calving are documented. Calving style was recorded with one or several of the following identifiers: (1) submarine: iceberg rises buoyantly from below the waterline, rather than falling from above, (2) subaerial topple: intact serac or large serac pieces rotating out from the terminus, generally pivoting near the water line, prior to impact with the fjord, (3) subaerial drop: intact serac or large serac pieces falling straight down from the terminus, (4) loose ice avalanche of small, broken ice debris, (5) sudden "gunshot" event, heard but not seen, (6) rumble event, heard but not seen, and (7) not associated with Yahtse Glacier: glaciers and icebergs overturning in other parts of the fjord occasionally produce audible events.

[14] The qualitative iceberg size was intended to describe the volume of ice involved in a calving event and is an integer with a minimum value of 1. This size scale is similar to that of *O'Neel et al.* [2007], is non-linear and intended to be approximately logarithmic. Although this scaling is subjective, it provides a useful classification of larger vs. smaller events. Size 1 events are no more than roughly 15 m tall, 20 m wide and 10 m deep (in the along-flow direction). Size 3 events may incorporate the entire height of the glacier terminus (50–60 m), be 30 m wide and 20 m deep. The typical size 5 event incorporates the entire subaerial terminus height, is 200 m wide and 50 m deep. Calving events at Yahtse Glacier tend to be smaller than those of Columbia Glacier, Alaska. Therefore, this size scale is finer than that

used by *O'Neel et al.* [2007], for whom a size 1 was equivalent to a 3 or 4 by the scale used in the present study. The largest size event observed at Yahtse during the observation period was assigned a 7. We assigned sizes to audible-only events based on the visible volumes of ice involved in similar sounding events.

[15] Event duration is an estimate for the amount of time during which the calved ice motion is substantially vertical, i.e., during free fall or buoyant rise, or while sound was audible. Timing was kept with a watch synchronized to the second with a handheld GPS unit. Four people contributed to the 81 h of observations, typically in 1 or 2 h shifts. Overlap between shifts, and several hours of training when two observers were present helped to maintain consistency throughout the record. These shift overlaps and comparisons of the simultaneous records do not reveal any clear biases among the different observers.

3.3. Video and Time-Lapse Photography

[16] Between 6–11 September 2010, 8.4 h of video were recorded of the terminus from Camp (Figure 2). Video was recorded with a Canon EOS 7D digital camera, shooting at 29.97 frames per second. Absolute timing was kept with a handheld GPS that was occasionally passed into the frame of the video so that the time on the screen was visible for several seconds. Following fieldwork, we made repeat measurements of the lag between the handheld GPS time and UTC, as reported by a millisecond-accurate clock. The lag of 14 comparisons made over two months approximated a normal distribution with a mean of 0.01 s and a standard deviation of 0.44 s. However, additional errors arise when we synchronize seismic data with these videos in the sections that follow. Thus we conservatively consider our video (with 0.033 s precision) to be synchronized via GPS to UTC (and the seismic data) with an accuracy of <1 s [see also *Wety et al.*, 2012].

[17] Three digital SLR cameras were arrayed around the glacier terminus at the locations of the BOOM and DOST seismometers and at Camp. These cameras captured images of the terminus every 20 minutes during daylight hours for the duration of our 27-month project.

4. Results

[18] The combination of seismic data with a long time series of in-person, direct calving observations and high-frame-rate video allows us to investigate the relationship between iceberg calving and glaciogenic seismicity at both inter-event (minutes to days) and intra-event (seconds) timescales.

4.1. Inter-Event Timescales: Minutes to Days

[19] During the observer period, we recorded 4659 observed events at or within a short distance behind the Yahtse terminus, at an average rate of one per 63 s (Figure 3). An additional 134 events were heard to originate from Guyot or other glaciers, or from within Icy Bay, apart from the Yahtse terminus. We discard these non-Yahtse events for the purposes of this study. Of the Yahtse events, 36% were seen; the others were only heard. The rate at which events occurred was not steady; strong variations in event rate were apparent at both hourly and multiday

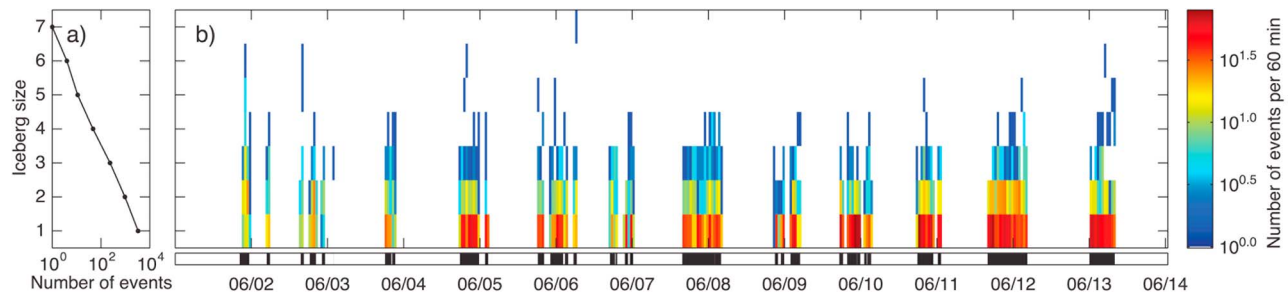


Figure 3. Observed events at the terminus of Yahtse Glacier during 12 days of observation, June 2010 (UTC time). a) Total number of events observed per iceberg size (Table 2). b) Event rate over the 12 day observer record per iceberg sizes, where the color scale represents the event rate on a logarithmic scale. The black bars at the base of the figure identify periods during which an observer was present.

timescales. Calving events also clustered spatially along the face of the terminus. Many calving events would occur in succession at one location over a period of 10 minutes or more while other regions of the terminus were quiet. Only 2.4% of calving events involved iceberg releases from below the sea surface (submarine events), although these tended to involve larger icebergs than subaerial calving events (similar to other observations [Motyka, 1997; O’Neel et al., 2007]). Frequently, submarine events were part of a longer, more complicated sequence of calving that also included subaerial components [Motyka, 1997]. Tables 1 and 2 present a summary of the observer record.

[20] The simultaneous operation of our seismic network with the observer record allows us to identify relationships between calving events observed at the terminus of Yahtse Glacier and icequakes (Figure 4). This comparison and others like it reveal several interesting patterns:

[21] 1. Approximately 75% of seismic events have a near-synchronous observed terminus event in the observer record. However, the converse is not necessarily true; many brief (<5 s), small size (≤ 2) observed events do not have coincident seismic events identifiable above the background seismicity. Time lags on the order of 15 s between the onset of an icequake and its associated calving event most likely reflect inaccuracy by the human observers. 2. Almost every visually observed, subaerial calving event (i.e., avalanches, drops, and topples) also has an associated seismic event. However, most of the audible-only events do not have a coincident seismic event. 3. Iceberg size and peak icequake amplitude are weakly related. 4. Topple events, which were generally observed to create the largest splashes as ice impacted the fjord surface, often are associated with the largest amplitude seismic events. For example, the largest

amplitude icequake in Figure 4 (at 11 June 2010 21:57) is associated with a relatively modest (size 3) topple event. 5. Submarine calving is associated with relatively low amplitude seismicity, unless the calving event was multipart and also had a drop or topple (i.e., subaerial) component. 6. The observer-recorded duration of terminus events correlates well with the duration of seismic events.

4.2. Intra-Event Timescales: Seconds

[22] The largest subaerial calving events at Yahtse Glacier are observed to involve brittle failure of the ice supporting the base of intact seracs. Visual inspection of 20-minute-interval time-lapse photographs taken perpendicular to the flow direction from the station BOOM reveal that seracs may slowly rotate top-out from the terminus for up to 4 h prior to calving. In addition to intact serac release, calving occurs as the release of interstitial ice from between less-damaged seracs and from the collapse of portions of seracs along pre-existing planes of weakness. However, the more closely one observes the terminus of Yahtse Glacier, the more continuous calving appears. Frequent small cracks and crumbles that are undetectable at kilometer distances are apparent at 100 m distances. More commonly, the human experience of calving is dominated by an awareness only of the infrequent, larger calving icebergs. Our observer record reflects this: discrete calving events punctuate relatively long-duration periods of quiet. While we document the largest calving events, there are undoubtedly many smaller events which we were unable to detect from our >0.5 km distance from the terminus.

[23] As at other glaciers, a large calving event at Yahtse Glacier may be viewed as the sum of many smaller contributing calving events [Qamar, 1988; Motyka, 1997].

Table 1. Number of Observer-Recorded Yahtse Terminus Events by Type^a

Event Type	Number of Events
Heard (“rumble”)	2814
Heard (“gunshot”)	305
Avalanche	219
Drop	1388
Topple	79
Submarine	112

^aA given terminus event may consist of multiple different types, and thus be present in the count for more than one event type.

Table 2. Number of Observer-Recorded Yahtse Terminus Events Per Size

Iceberg Size	Number of Events
1	3329
2	962
3	235
4	47
5	11
6	4
7	1

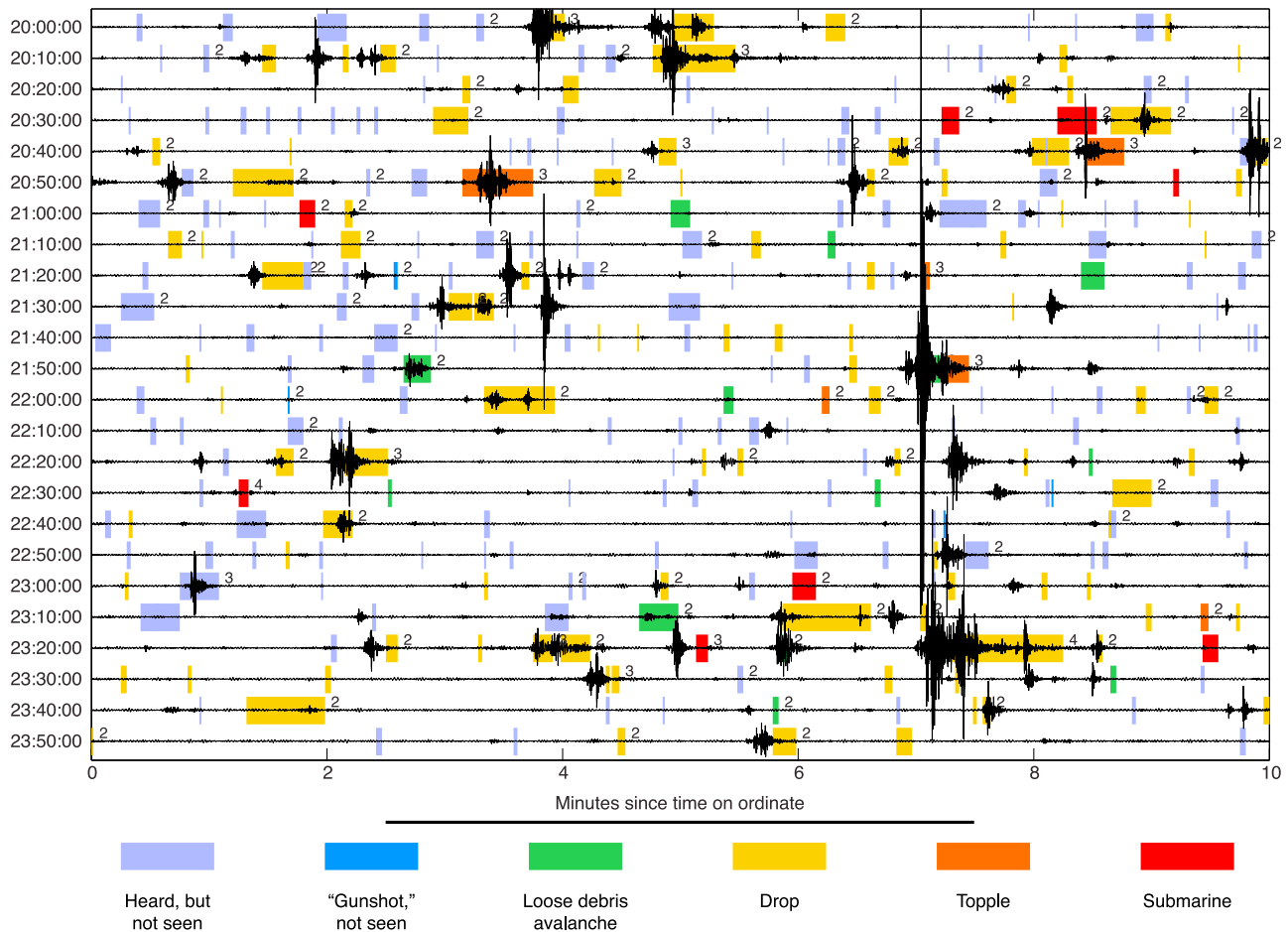


Figure 4. Four hours of seismic data with individual Yahtse terminus events from the calving observer record superimposed. Seismograms recorded on the vertical channel of BOOM (black lines) are shown, ten minutes per line, beginning 11 June 2010, 20:00:00 UTC, a time period with particularly frequent calving (Figure 3). The differently colored symbols represent different *styles* of terminus events. Although a single calving event may occur as a chain of linked events with different calving styles, only one *style* is identified per event. The hierarchy of styles used for plotting is as presented in the text, regardless of the temporal style order. That is, for an event that began as a subaerial drop, followed with a topple, and then ended with a loose avalanche, the event will be identified as a subaerial topple. Length of colored bar is the duration of the observed event. Observed iceberg sizes greater than one are identified with a number to the right of the colored bar. No earthquakes in the catalogs of the Alaska Earthquake Information Center or the USGS Preliminary Determination of Epicenters are visible in this figure. Seismograms are filtered between 0.5 and 5 Hz.

Furthermore, small calving events consist of several distinct parts. Small, subaerial calving events with iceberg size 1 or 2 (the most frequent calving events at Yahtse) have typical durations of 10 s and consist of (1) ice fracture and iceberg detachment, (2) iceberg fall and acceleration towards the water surface, (3) “crown” splash as the iceberg begins to displace water at the sea surface and decelerate, and, in some cases, (4) the creation of a high-speed, Worthington jet following complete submergence of the iceberg below the water surface [Gekle and Gordillo, 2010]. Larger calving events result from larger blocks of detached ice and the simultaneous or enchainned occurrence of several smaller events.

4.2.1. Synchronous Calving and Seismic Observations: ‘What Are the Mechanisms Responsible for Calving Seismicity?’

[24] To examine the sources and patterns of calving seismicity, we synchronized seismic data from the vertical channel of BOOM with video of 70 calving events. Of these, 57 events were sufficiently well-recorded by both video and seismometers to use in our analyses. Movies 1 and 2 give two examples.¹ For each of these calving events, we can track the icequake ground motion through our seismic network to 13 km distances. Relative to the extended durations of recorded icequakes, the observed dispersion is small; qualitative icequake duration recorded at a sensor 12 km from

¹Animations are available in the HTML.

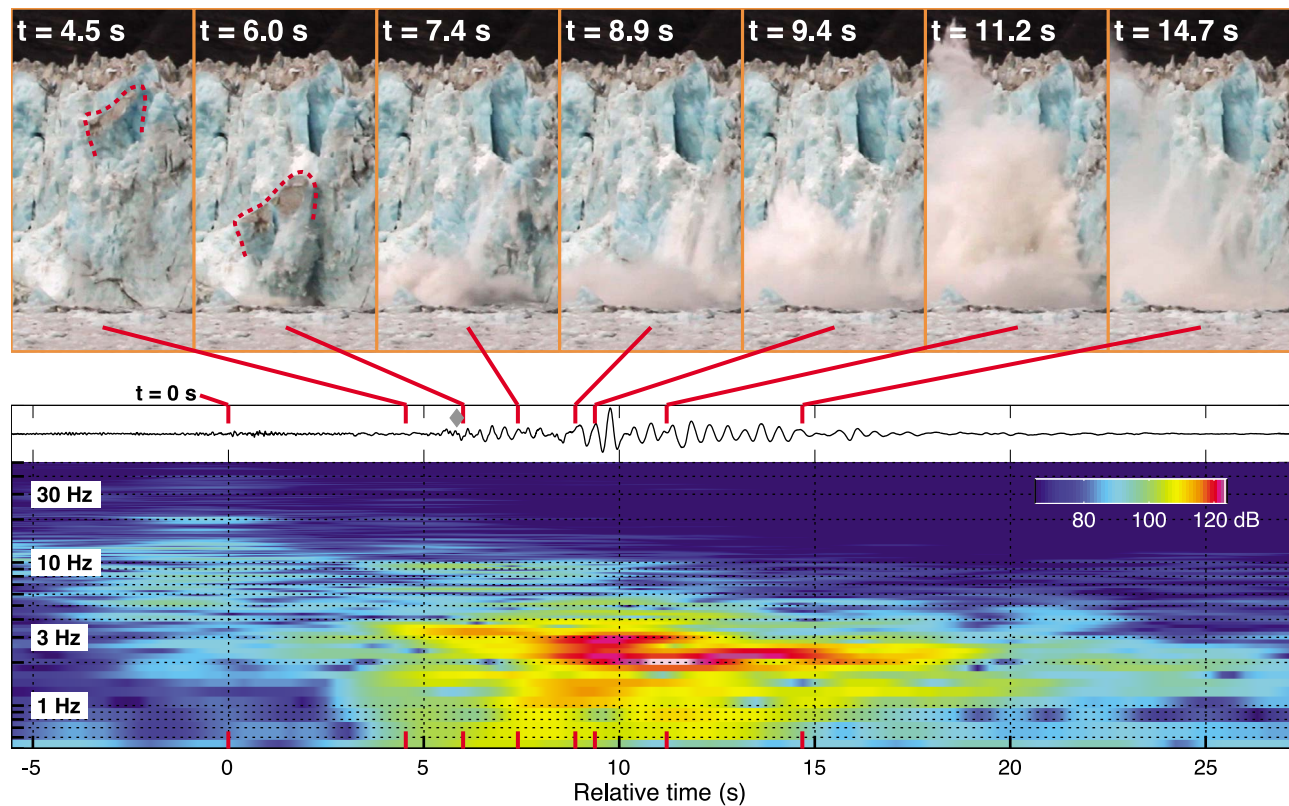


Figure 5. Video stills of calving event “Block” at the terminus of Yahrtse Glacier, unfiltered seismic waveform and spectrogram of waveform. Terminal cliff is approximately 60 m tall. Event has an iceberg size of 3 and a $18 \mu\text{m s}^{-1}$ maximum ground velocity on the vertical channel of BOOM. In the first two panels from video, the top of the major detached block is outlined with a red, dashed line. Ice associated with the calving event is observed to begin falling at 7 Sept 2010, 22:13:50.3 UTC ($t = 0$). The time of each video panel is identified in seconds relative to $t = 0$ and marked on the seismic data by vertical red ticks at the top of the waveform and bottom of the spectrogram. Seismic data has been shifted forward 0.95 s to correct for seismic wave travel time. A “step” in the icequake amplitude is identified with a gray diamond. At 8.8 s, a Worthington jet emerges from the fjord. The spectrogram presents the velocity of the sensor (in dB) as a function of frequencies between 0.5 and 50 Hz, as a function of time. Movie 1 shows video of this calving event, synchronized with the seismic data.

the source is approximately 1.5 times the duration recorded at BOOM, 1.8 km from the source. Thus, due to its proximity, the time series of ground velocities recorded at BOOM is largely controlled by the source time function. We time shift the recorded seismogram back to the origin time using the source-receiver distance and the average speed at which the maximum icequake ground velocity moves through our network (1.9 km s^{-1}). Although this is a rough estimate, the correction (≤ 1.1 s) is smaller or on par with errors in video timing and is far shorter than the event durations.

4.2.1.1. Two Example Calving Events

[25] To characterize our observations from the 57 calving events with synchronized seismograms and video, we present two simple, typical, well-recorded examples of different types of calving (Figures 5 and 6 and Movies 1 and 2). To discern if different mechanisms emit seismic energy in different frequency bands, we present spectrograms of seismic data surrounding each calving event.

[26] In the first example, which we refer to as “Block” (Figure 5 and Movie 1), a large, intact block falls from high on the terminus, entrains a small additional amount of ice

during its fall, creates a large crown splash, and then emits a Worthington jet that launches ice fragments over 100 m into the air, nearly twice the terminus height (visible in Movie 1). In this example, weak 4–15 Hz seismic signals precede and coincide with the release of several small ice fragments from around the largest iceberg block ($t = 0$ s). At 3.5 s, the initial small fragments begin to collide with the fjord surface at the same time as a rapid increase in lower-frequency 1–3 Hz seismic energy. Between 5.6 and 8.9 s, the rain of larger icebergs collides with the fjord surface and a “step” in the seismic amplitude occurs, with peak power between 1 and 4 Hz. Additional lower-amplitude seismic signals between 6 and 10 Hz coincide with these impacts. At 8.8 s, the Worthington jet erupts from the fjord surface with greater velocity than the splashing observed previously. At 9.0 s, the amplitude of the low frequency 1–3 Hz seismic waves increases yet again and the unfiltered seismic waves reach their maximum amplitude, $18.3 \mu\text{m s}^{-1}$, at 9.7 s. By 10.5 s, all debris has completely fallen from the terminus, but seismic amplitudes between 0.6 and 4 Hz remain strong. A protracted coda eventually approaches background levels

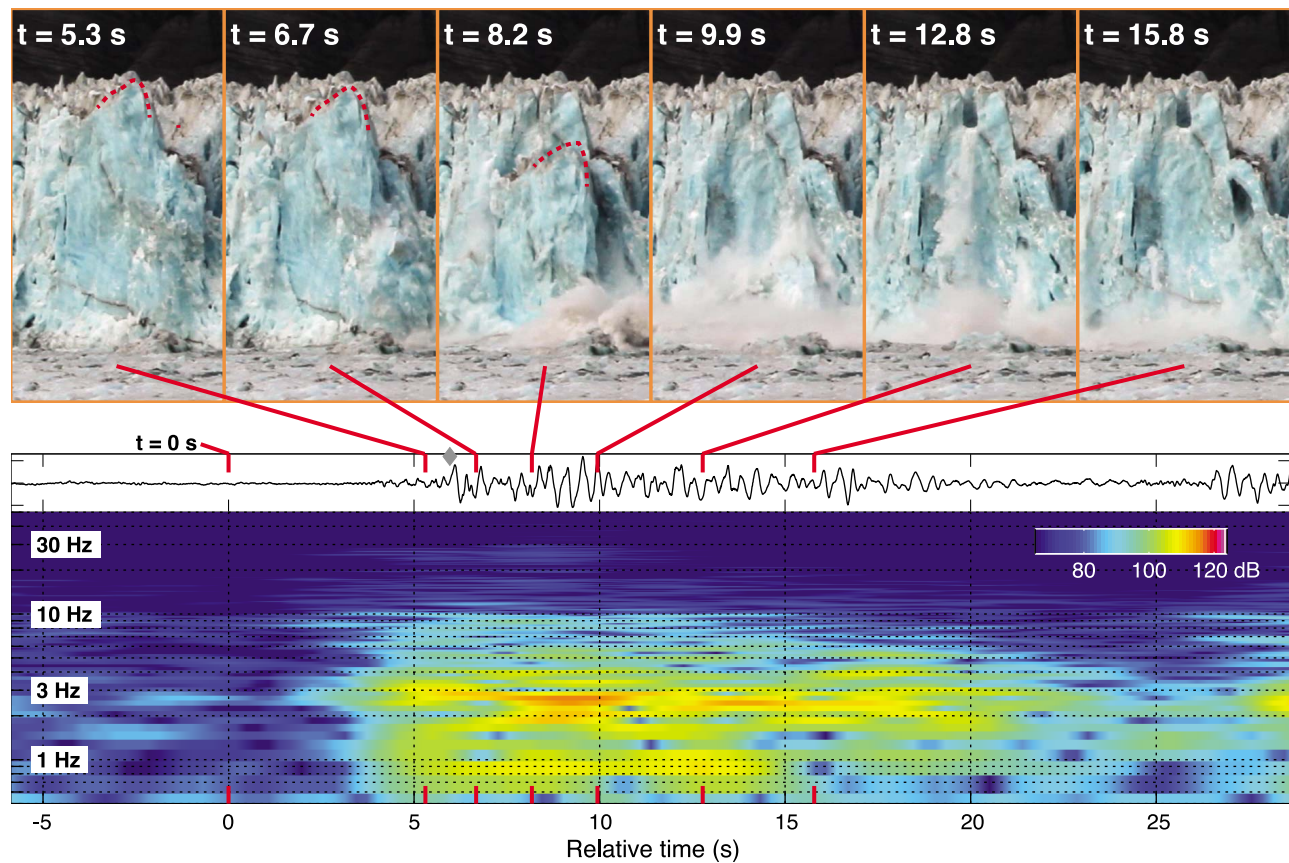


Figure 6. Same data types as presented in Figure 5, but for example calving event “Flake.” Event has an iceberg size of 4 and a $6 \mu\text{m s}^{-1}$ maximum ground velocity. In the first three panels, the top of the collapsing serac/flake is outlined with a red, dashed line. Ice associated with the calving event is observed to begin falling at UTC 7 Sept. 2010 23:17:51.6 ($t = 0$). No Worthington jet is associated with this calving event. Seismic data has been shifted forward 0.94 s to correct for seismic wave travel time. Movie 2 shows video of this calving event, synchronized with the seismic data.

at around 20 s. The amplitudes between 2 and 3 Hz exceed the amplitudes at other frequencies throughout the duration of the calving event by 20 dB.

[27] In the second example, which we refer to as “Flake” (Figure 6 and Movie 2), an entire, intact serac-flake collapses from the terminal cliff. The volume of calved ice in Flake appears to be twice that of Block (Figure 5) and, although crown splashing is present, no Worthington jet is observed. This calving event initiates with the release of several small ice fragments, barely visible in the recorded video ($t = 0$ s). No significant seismicity is coincident with these small releases. At 4.0 s, ice on the right-hand-side of the intact flake crumbles and breaks away, coincident with the initiation of weak seismicity at frequencies that span the range from 0.5 to 10 Hz; ice on the left-hand side follows at 4.9 s. At 6.0 s, the large, intact flake begins to fall and at 6.3 s, water at the base of the flake is seen displaced by the collapsing flake. These events are coincident with an increase in energy across a range of frequencies, although ground motion near 3 Hz is approximately an order of magnitude greater than that at other frequencies. Between 6.7 and 7.9 s, crown splashing associated with the impact of the right-hand-side ice is seen in the video and the peak frequencies spread down to include 1.5 Hz. Crown splashing

and a surge of water spreads to the left along the terminus while the ground velocity peaks at 9.5 s ($5.9 \mu\text{m s}^{-1}$, one third the peak amplitude of Block). At 11.4 s, the top of the large flake has slipped below the sea surface and the largest splashes have concluded. Thereafter, several more moderately sized ice fragments fall from the same region of the terminus until 23 s, during which time the 1.6–4 Hz coda slowly decreases in amplitude. A second wave of calving, including another flake similar in size, shape and location to the first flake, begins at 24.6 s.

4.2.1.2. Common Characteristics of Calving Icequakes

[28] The two calving events and icequakes described above are representative of Yahtse’s calving seismicity (Figure 9). Nearly all of the well-recorded calving icequakes recorded at BOOM lack clear P - or S -wave arrivals and have 5–30 s durations, emergent onsets, and relatively constant low-amplitude early portions that typically “step” to larger amplitudes. In Block, Flake, and almost all of the calving icequakes, the seismic amplitude in the frequency band from 0.5 to 5 Hz (peaked near 3 Hz) exceeds the amplitude at higher frequencies (see section 4.2.2). Below 0.5 Hz, icequake amplitude appears to decrease, although we are limited from examining these lower frequencies by the presence of ocean microseism between 0.1 and 0.5 Hz [Stein and

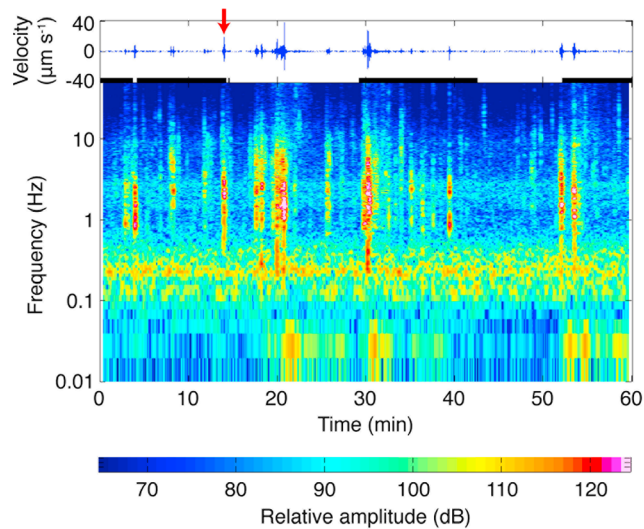


Figure 7. One hour spectrogram from the vertical channel of BOOM, starting 7 Sept. 2010 22:00:00 UTC. Video of the terminus was recorded during the time period identified with the black band between the seismogram and spectrogram. The icequake generated by example event Block (Figure 5) is marked with the red arrow. Inspection of video and an observer record reveal that most of the other icequakes can also be associated with calving events. Decibel scale is the same as in Figures 5 and 6.

Wysession, 2003] (Figure 7). The largest amplitude seismic waves very often correlate in time with interactions between icebergs and the sea surface (Figure 8). Worthington jets appear in 30 of our 57 calving events after largely intact blocks of ice fall from high on the terminal ice cliff and briefly submerge below the sea surface. In these cases, the time of jet eruption coincides well with the time of the peak seismic amplitude (Figure 8a), often 5 s after the iceberg initially hits the fjord surface and the crown splash forms.

[29] Seismic waves at 1–5 Hz frequently exhibit a “step” in their amplitudes and energy early in the evolution of the icequake, when the seismic amplitude may double or more (equivalent to an increase of >6 dB, Figure 9). Steps in icequake amplitude are also present at $t = 5.8$ s for Block and $t = 5.9$ s for Flake (Figures 5 and 6 and Movies 1 and 2). These steps occur with or without jets, were coincident with the biggest splash of the iceberg (the crown splash) and typically lag the detachment of the iceberg from the glacier’s terminal cliff by 2 to 4 s (Figure 8b). Seismic waves at 0.5–5 Hz are also associated with iceberg detachment, but these waves are lower amplitude than those related to iceberg splashing.

[30] Seismic waves at greater than 5 Hz are associated better with ice crumbling and fracturing than with splashing, and almost always at least 10 dB weaker than lower frequency energy. However, calving events that create small splashes have commensurately weak seismic waves between 0.5 and 5 Hz. In these cases, the amplitude of higher frequency seismic waves can equal that of the lower frequency waves.

4.2.2. Frequency Content of Calving Icequakes

[31] In both the Block (Figure 5) and Flake (Figure 6) examples, the amplitude of ground motion between 1 and

3 Hz exceeds that at higher frequencies. The spectra of these two examples are shown in Figure 10, along with the spectra from a set of local, tectonic earthquakes and a period during which no calving events are observable in the video and no clear seismic events occurred. The 10 earthquakes have magnitudes $1.0 < M_L < 1.5$ and are located within 30 km of BOOM by the Alaska Earthquake Information Center. Block, Flake and the earthquakes each have seismic energy at levels greater than that of background for all observed frequencies. However, the shapes of the earthquake and icequake spectra have clear differences. Relative to the earthquakes, the icequakes have comparable seismic amplitudes between 5 and 10 Hz and have lower amplitudes between 10 and 20 Hz. The two icequakes are most different from the earthquakes in the frequency range between 1 and 3 Hz, where the spectra exceed the median earthquake amplitude by an order of magnitude or more. This result is consistent with previous studies that have associated strong 1–3 Hz seismicity with iceberg calving [Wolf and Davies, 1986; Qamar, 1988; O’Neil et al., 2007; Walter et al., 2012].

[32] Throughout the spectra, including within the 1–3 Hz band, Block and Flake have multiple, distinct peaks of nearly equal amplitude, as do the earthquakes. The presence of these multiple spectral peaks was common among the 57 calving events for which video was recorded. The

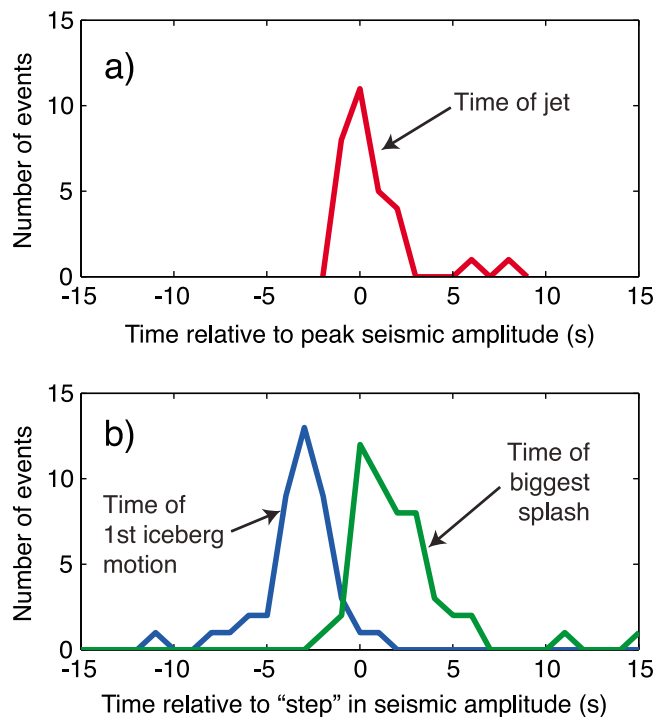


Figure 8. Time lags between video events and seismic events, rounded to the nearest second. (a) Time lag between the peak seismic amplitude and Worthington jets visible in the video. Thirty jets associated with calving events were identified. (b) Time lag between large amplitude “step” in the seismic amplitude and (at left) the first motion in the video of the large collapsing iceberg, and (at right) the largest splash of the calving event. Steps are a common feature of the calving icequake waveforms (Figures 5, 6 and 9).

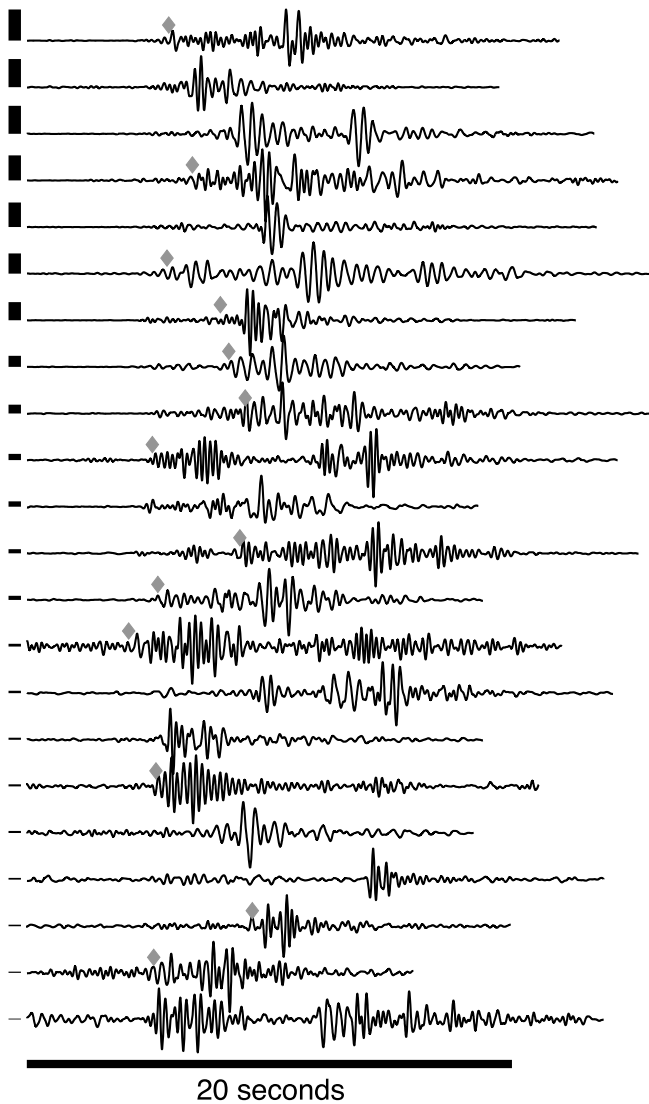


Figure 9. Example icequakes resulting from subaerial calving events in the observer record. The third icequake from the bottom is the result of a topple event. All others resulted from drop calving events. Events occurred between 20:00 and 21:00, 11 June 2010, the first hour of the data presented in Figure 4. Seismograms were recorded on the vertical channel of BOOM and are shown filtered between 1 and 5 Hz. Icequake amplitudes are normalized, with the relative amplitude of each event indicated by the height of the vertical black bar to the left of the icequake. The top seismogram, with the largest amplitude, reaches a peak of $22 \mu\text{m s}^{-1}$. Gray diamonds above many of the seismograms identify “steps” in the seismic amplitude that are discussed within the text.

specific frequencies of 1–3 Hz peaks and troughs vary among our recorded calving events, with no persistent maxima or band gaps. Among the video-recorded calving events, the median peak frequency was 2.3 Hz with an interquartile range of 0.7 Hz; 92% of calving events had a peak frequency between 1 and 5 Hz. Across our network, the value of this peak frequency decreased only slightly (≤ 0.5 Hz) as the seismic waves traveled the 12 km out from terminus.

[33] None of the calving events observed were of sufficient size or duration to generate seismicity such as the glacial earthquakes reported in *Ekström et al.* [2003] and elsewhere. However, ground motion with 25–50 s periods was detected above background levels at BOOM 1 to 3 minutes after many icequakes with amplitudes in excess of $10 \mu\text{m s}^{-1}$ (Figure 7). The source of this ground motion is different than that described in *Tsai et al.* [2008] and *Amundson et al.* [2010]. For events with simultaneous video, these long-period seismic waves coincided with the arrival of water waves with comparable periods arriving on the shore. These earth-loading signals are absent from stations more distant from the shoreline. Some long-period signals exhibited dispersion, consistent with the arrivals of surface (water) waves [*Amundson et al.*, 2008, 2012].

5. Discussion

5.1. Contributions to the Seismicity of Yahtse Glacier

[34] Based on an examination of Figure 4 and other figures like it, iceberg calving at Yahtse Glacier dominates the locally recorded seismic wavefield and can be conclusively identified as the source of at least 75% of icequakes recorded near the glacier terminus. In actuality, given the consistent appearance of most of the waveforms (see section 4.2.1.2) and considering that only 60% of the terminus was visible from our observation point, the calving contribution to the local seismic wavefield may be even greater.

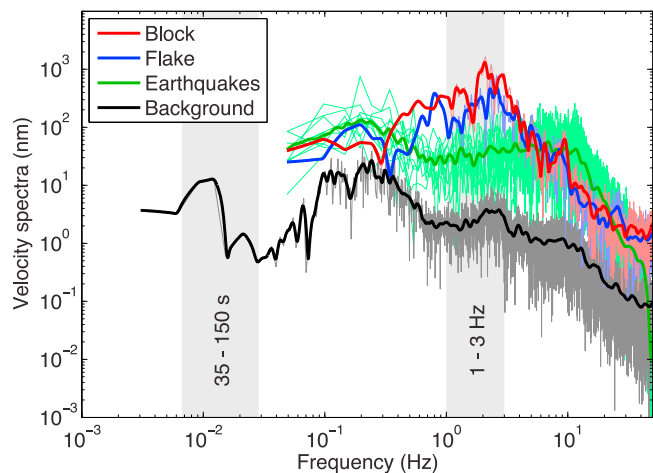


Figure 10. Velocity spectra from the two calving events displayed in Figures 5 and 6, compared with local earthquakes and background seismicity. Ten local earthquakes within the magnitude ranges of $1.0 < M_L < 1.5$ are shown in pale green. Smoothed spectra are displayed bold on top of the unsmoothed spectra; the earthquake spectra have been stacked prior to smoothing. Durations for which spectra are displayed are 18 s for the Block, 19 s for the Flake, 20 s for each earthquake and 300 s for background. All waveforms are from the vertical channel of BOOM, as reported elsewhere. The BOOM sensor has a flat response to seismic signals between 0.008 and 50 Hz. Two gray-shaded rectangles identify the frequency ranges discussed in previous studies of glacial earthquakes [e.g., *Ekström et al.*, 2003] and icequakes [e.g., *O’Neel et al.*, 2007].

[35] Within a single calving event, interactions between the iceberg and the fjord surface (i.e., splashing, jetting) are the most seismically energetic sources. In particular, cavitation (identified by the occurrence of Worthington jets created by collapsing air cavities) is the mechanism identified with the greatest potential for large amplitude seismic waves (Figures 5 and 8a). This mechanism, with the entrainment of a cavity above the plunging iceberg and the subsequent collapse of an enclosed air bubble, is akin to the firing of air guns, commonly used in marine seismic surveys as an active seismic source [e.g., *Stein and Wysession, 2003*].

[36] The association between iceberg–sea surface interactions and high amplitude icequakes offers a potential explanation for the lack of coincidence between audible-only terminus events and icequakes (Figure 4). Many of these audible-only terminus events sounded as though they originated from behind Yachtse Glacier’s terminal cliff. We suspect that these audible-only events were generated by serac collapse within the highly crevassed lower reach of Yachtse Glacier. If the falling serac ice blocks never impact the fjord surface, then they do not splash nor lead to cavitation beneath the water surface—the mechanisms of strongest icequake generation in our study.

[37] These observations further support the conclusions of *O’Neel et al. [2010]*: calving is the source of the concentrated epicenters at the head of Icy Bay. Thus, not only are ice–water impact and cavitation the most seismically energetic parts of iceberg calving, they appear to be the most common and efficient icequake generators of any glaciological process active within the ice-rich and glaciologically diverse St. Elias Range of Alaska and Yukon Territory. Yachtse Glacier produces smaller icebergs than other Alaskan Glaciers, where $>2 \times 10^6 \text{ m}^3$ of ice can be released in a single calving event [*Motyka, 1997; O’Neel et al., 2007*]. We propose that the relative stability of this grounded, advancing glacier (shallow, 110 m, water depth and terminus height ~ 45 m above its flotation threshold) limits the maximum size of individual calving events. This height above buoyancy is close to the level observed previously for stable tidewater termini [*van der Veen, 1996*]. Closely spaced crevasses and crevasse penetration through the entire subaerial portion of the terminus serve to further limit the maximum size of calving events. In spite of these limitations on calving event size, Yachtse Glacier remains a regional “hot spot” of icequake occurrence due to the high occurrence rate of icebergs falling from high on the glacier terminus.

[38] Fjord interaction mechanisms are certainly not the only seismogenic mechanisms associated with iceberg calving. We record relatively weak seismicity at frequencies >5 Hz often associated with the earliest parts of a calving event, including during and preceding iceberg detachment and clearly before any apparent splashing. Energy at these higher frequencies is particularly strong in calving events with significant crumbling and avalanching character, supporting previous research that suggests high frequency seismicity in glacial environments is related to ice fracturing [*Neave and Savage, 1970; Deichmann et al., 2000; Walter et al., 2008; Carmichael et al., 2012*].

[39] We do not discount potential contributions from the other mechanisms listed in the introduction, including basal slip, subglacial conduit hydraulics, grinding of ice mélange,

unloading of the remaining ice surface, or resonance of water filled–fractures or of free-standing seracs. Indeed, relatively low-amplitude, 0.5–5 Hz seismicity coincident with iceberg detachment is common. In the present work, we are unable to identify the exact source of this early part of the calving waveforms (that beginning at $t = 3.3$ s and $t = 4.8$ s in Figures 5 and 6), but vibration of water-filled cracks [*Métaxian, 2003; O’Neel and Pfeffer, 2007; Winberry et al., 2009*] or the remaining serac, or friction and/or collisions between the falling block and the terminal cliff remain possibilities.

5.2. Source Mechanisms

[40] We envision four mechanisms by which icebergs could interact with the sea surface to generate seismic energy. These are sequentially: (a) the moment of impact of an iceberg on the fjord surface, when momentum is rapidly transferred from the falling iceberg to the seawater, (b) the deceleration of the iceberg through the water, under the influence of drag and buoyancy, (c) in the case of complete submergence of the iceberg below the sea surface (i.e., cavitation), the inward acceleration and collapse of the walls of the below-sea-surface air cavity, and (d) the moment of air cavity pinch off, when the water walls, all moving radially inward, contact each other, accelerate outward, and generate a Worthington jet (Figure 1). Slamming (mechanism (a)) will only occur in the case of subaerial calving; however iceberg deceleration and cavitation seismogenesis can also occur during submarine calving, particularly if a rising iceberg has sufficient momentum at the sea surface to carry it substantially above its position of hydrostatic equilibrium. This is most likely to occur at tidewater termini in deep fjords [e.g., *Motyka, 1997; O’Neel et al., 2007*].

[41] The timescales for these four mechanisms vary from nearly instantaneous impulses, (a) and (d), to longer-duration mechanisms that evolve over tenths to whole second durations, (b) and (c). The more impulsive mechanisms may generate ground motion across a wide range of frequencies, just as a Lamb pulse or delta function contains energy at all frequencies [e.g., *Kanamori and Given, 1983*]. The three-dimensional structure of our field site, including soft, glaciomarine mud that blankets the fjord bottom, has the potential to trap and amplify some frequencies of seismic waves [*Kennett, 2002*]. However, further exploration of these path effects would tell us more about geologic structure and the transmission of seismic waves than about the seismic source. Thus, we focus on the iceberg deceleration (b) and cavity collapse (c) mechanisms. If the forces associated with iceberg deceleration and cavity collapse act over durations similar to half the wave period at the peak seismogram amplitude, then we gain confidence that this mechanism may be a significant part of the icequake source [*Stein and Wysession, 2003*].

5.2.1. Setup of Hydrodynamic Model

[42] We first consider the vertical deceleration forces on an idealized, vertical, cylindrical iceberg, with bottom radius R and height H (mechanism (b), above). We define z as the height of the iceberg bottom above the water surface. Thus, $m = \rho_i H \pi R^2$ is the mass of the iceberg, where ρ_i is the ice density, 917 kg m^{-3} . During iceberg impact on the fjord surface, the iceberg will transfer some of its momentum to the water (mechanism (a)), and accelerate that water along

its downward trajectory. The mass of the entrained water is accounted for as an *added mass*, m_a , which is defined for periodic motion of a solid object within a fluid [Sabunco and Calisal, 1981; De Backer et al., 2009]. For the case of abrupt impact, the high frequency limit is appropriate. The expression for the added mass of a normally incident, impacting, vertical cylinder is:

$$m_a = 0.37\pi\rho_w R^3 \quad (1)$$

[Korotkin, 2009; Sabunco and Calisal, 1981], where ρ_w is the density of seawater (1014 kg m⁻³ for temperature and salinity conditions near the terminus of Yachtse Glacier (T. C. Bartholomäus, unpublished hydrographic data, 2011)).

[43] The equation of motion is

$$\frac{d}{dt}(m + m_a)U = mg - F_B - F_D \quad (2)$$

or equivalently

$$(m + m_a)\frac{dU}{dt} = mg - F_B - F_D - U\frac{dm_a}{dt} \quad (3)$$

where U is the iceberg velocity, dz/dt , g is the gravitational acceleration, F_B is the buoyancy force, and F_D is the drag force. The relative importance of surface tension and inertia is given by the Weber number, which in this case indicates that surface tension is negligible. The buoyancy and drag forces are defined as

$$F_B = \rho_w(W_r\pi R^2 H)g \quad (4)$$

where W_r is the wetted ratio of the iceberg height, between 0 and 1, and, for $z < 0$,

$$F_D = \frac{1}{2}C_D\rho_w\pi R^2 U|U|, \quad (5)$$

where C_D is the drag coefficient. The drag coefficient depends on the shape and roughness of the iceberg and on the nature of the water flow around the iceberg, typically described by the non-dimensional Reynolds, Re , and Froude, Fr , numbers [e.g., May and Woodhull, 1948; Gaudet, 1998; Goossens, 1987]:

$$Fr = \frac{U^2}{gR}, \quad Re = \frac{UR}{\nu} \quad (6)$$

where ν is the kinematic viscosity of water. For an iceberg with $R = 8$ m, after free fall from a height of 20 m, $Re = 9.5 \times 10^7$ and $Fr = 5$ at the moment of impact. Although the values of Re and Fr , and therefore C_D , will change as the iceberg begins to decelerate, we are most interested in the first seconds after impact, when the drag force is greatest. Furthermore, C_D is substantially controlled by the location on the iceberg where laminar flow separates from the iceberg surface and turbulence initiates. For a smooth, circular disk pressed through a fluid, Batchelor [1967] reports that the location of this flow separation is fixed at the sharp disk edge for $Re \gtrsim 3 \times 10^3$, and thus C_D (with a value of 1.1) is independent of Re . Therefore, for our envisioned rough, angular icebergs, we select one value of

C_D and hold it constant for the duration of each model run. Based on results from dimensionally similar experiments [e.g., Aristoff et al., 2010; Gaudet, 1998; Glasheen and McMahon, 1996] and the knowledge that the drag for rough, irregularly shaped icebergs is greater than that for idealized objects [Hottovy and Sylvester, 1979; Goossens, 1987], we test our model with $C_D = \{1, 2, 4\}$.

[44] The $-Udm_a/dt$ term of equation (3) is often regarded as a “slamming” force in the water-entry literature [Miloh, 1991; De Backer et al., 2009] and is equivalent to mechanism (a). Particularly for blunt objects, this slamming force may be of very large magnitude but brief duration—typically on the order of several milliseconds. We prescribe a radial, hemispherical growth of m_a at the pressure wave velocity α for brackish seawater, 1470 m s⁻¹. For the short time interval while m_a grows to its full value (equation (1)),

$$\frac{dm_a}{dt} = \rho_w 2\pi r^2 \frac{dr}{dt}, \quad (7)$$

where r is the instantaneous radius of added mass, i.e., the fluid entrained by the iceberg, and

$$m_a = \rho_w \frac{2}{3}\pi\alpha^3 t^3. \quad (8)$$

The expression for $\frac{dm_a}{dt}$ need not be exactly of the form of equation (7); however, the large ratio of α / U ensures that the slamming force associated with momentum transfer from iceberg to water occurs over millisecond timescales, as identified in studies with other objects [Miloh, 1991; De Backer et al., 2009].

5.2.2. Model Results and Interpretation

[45] The numerically integrated results of equation (3) are presented in Figure 11. Approximately 2 s prior to impact ($t \sim -2$ s), an iceberg ($H = 10$ m, $R = 8$ m) detaches and begins free-fall from 20 m, impacting the fjord surface at $t = 0$ s. On impact, the net force on the iceberg abruptly switches from body-force-dominated, with negative net force, to slamming- and drag-force-dominated, with positive (upward directed) net force (Figure 11a). Within 5 milliseconds, the slamming force associated with the entrainment of seawater peaks at 6000×10^6 N and the iceberg reaches a peak acceleration of 2500 m s⁻². Once m_a has reached its maximum value, the slamming force vanishes and the net force is dominated by the drag force; iceberg acceleration falls to 45 m s⁻². The net slamming impulse (equivalent to the change in momentum) is given by

$$\int_0^{5\text{ms}} U \frac{dm_a}{dt} dt = \Delta Um_a = 1.0 \times 10^{12} \text{ N s}, \quad (9)$$

and is roughly half that of the impulse imparted by the drag force,

$$\int_0^{\tau_d} F_D dt = 2.1 \times 10^{12} \text{ N s}, \quad (10)$$

where τ_d is the timescale over which the seismic source is expected to act, defined within the following paragraph. Slamming has the potential to act as a Lamb pulse on the water surface and contribute to the icequake signals recorded

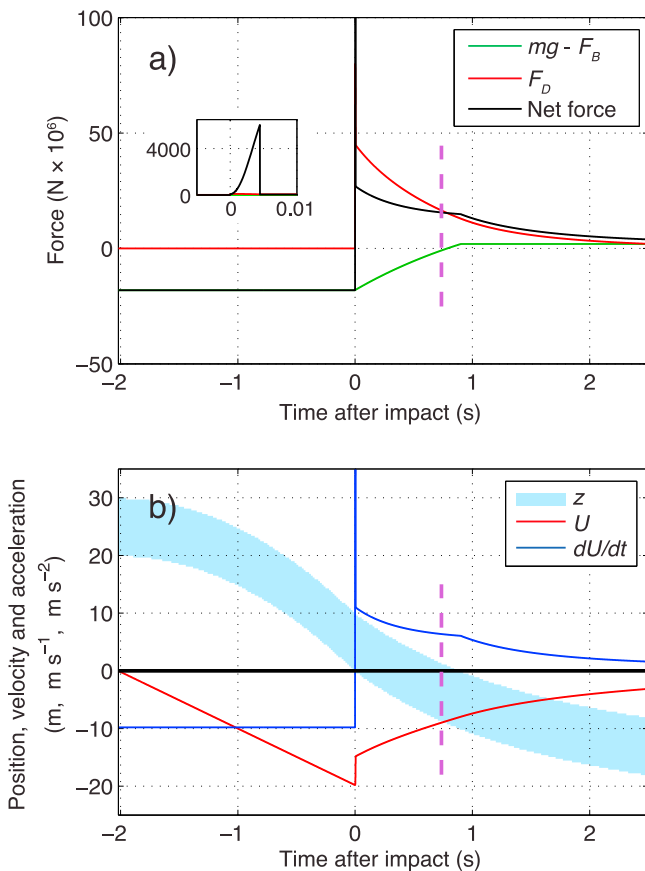


Figure 11. Results of the hydrodynamic model for an iceberg ($H = 10$ m, $R = 8$ m) falling into a fjord. (a) Total body force, drag force ($C_D = 2$), and sum of forces acting on the iceberg (right-hand side of equation (3)). Inset shows the slamming force. Axes labels as in main plot. (b) Vertical position (z , shaded band), velocity and acceleration of the iceberg resulting from the forces of Figure 11a. Vertical, dashed, purple lines identify $\tau_d = 0.74$ s: that time by which most of the drag force has been imparted to the iceberg.

at our seismometers [e.g., Kanamori and Given, 1983]. However, the transmission of these waves will be hampered by water’s inability to transmit shear waves and complicated by unquantifiable path effects. Thus, while acknowledging that slamming may contribute to our icequake signals, we focus the discussion on the longer duration evolution of the iceberg motion.

[46] As the calved iceberg and entrained fluid ($m + m_a$) decelerate under the influence of drag, the drag force decreases (equation (5)). In the example presented here, the model results are truncated at 2.5 s because the choice of large, constant C_D becomes inappropriate at large t due to the C_D dependence on Re and Fr . As the iceberg approaches zero velocity at the nadir of its trajectory, the drag force decays towards zero. However, due to the gradual decay of F_D , we do not anticipate that the time to $F_D = 0$ is the relevant timescale for the seismic source. Instead, we select the deceleration timescale to be the e -folding time τ_d , i.e., the time by which F_D has fallen to $1/e$ of its maximum value.

This definition of τ_d is somewhat arbitrary; however, the value of τ_d in this and other examples is fairly insensitive to its definition.

[47] With τ_d as the approximate duration of the icequake source, $f_d \sim 1/(2\tau_d)$, where f_d is the icequake frequency measured by a seismometer [Stein and Wysession, 2003]. In the case of Figure 11, $f_d = 0.7$ Hz. Figure 12 illustrates the relationship between f_d , iceberg height and the drag coefficient. The icequake frequency depends on other parameters as well. If R is nearly doubled to 15 m, the resulting values of f_d decrease by approximately 50%. If the initial free-fall height of the iceberg is doubled from 20 m to 40 m, f_d increases by approximately 50%. For a wide variety of iceberg sizes and fall heights, we may expect that iceberg deceleration after impact has the potential to create seismic signals with frequencies between 0.5 and 2 Hz. These frequencies are slightly lower than we have observed at Yahtse Glacier, but given the simplicity of our model, they are remarkably close to the frequencies of observed calving icequakes. Iceberg deceleration is a potential explanation for the observed “steps” in the strength of low-frequency seismic amplitude that are associated with icebergs splashing and decelerating into the fjord.

[48] In Figure 11, cavitation begins at $t = 0.9$ s, after the top of the iceberg has descended below the sea surface. Although cavitation is not accounted for in the one-dimensional equation (3), we can apply a similar hydrodynamic analysis to the case of cavity wall collapse (mechanism (c)). Cavity collapse immediately precedes cavity pinch-off and the eruption of the Worthington jet (mechanism (d)) that coincides with peak amplitudes in calving icequakes. An air cavity formed after water impact in the lee of a descending object will pinch off at a location largely controlled by the value of Fr . In our cases, where surface tension may be neglected and the density of the object is approximately equal to the density of the fluid, $\frac{z_c}{R} \sim Fr^{1/2}$, where z_c is the depth below the water surface at which the cavity first pinches off [Gaudet, 1998; Gekle et al., 2008; Bergmann et al., 2009].

[49] The difference in potential energy between the surrounding water surface and the pinch-off depth of the fully

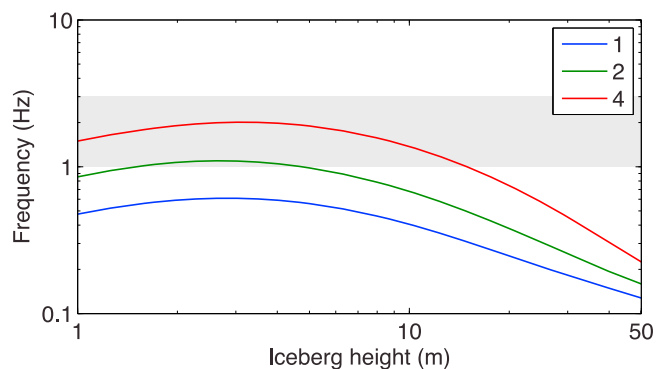


Figure 12. Dependence of the icequake frequency, f_d , on iceberg height, H , and a range of plausible drag coefficients $C_D = \{1, 2, 4\}$. $R = 8$ m and the iceberg free-fall height is 20 m for all cases. Gray shaded box identifies $1 \text{ Hz} \leq f_d \leq 3 \text{ Hz}$.

open cavity, z_c , is approximately equal to the kinetic energy of the collapsing cavity walls at the moment of pinch-off:

$$V\rho_w g z_c \sim \frac{1}{2} V\rho_w \left(\frac{R}{\tau_c}\right)^2, \quad (11)$$

where V is the cavity volume and τ_c is the cavity collapse timescale. When we rearrange equation (11) and eliminate z_c , this reduces to

$$\tau_c \sim \sqrt{\frac{R}{2gFr^{1/2}}}. \quad (12)$$

If we apply the particular parameters and geometric values used in Figure 11 again, then $\tau_c \sim 0.43$ s. As above, we define an icequake frequency $f_c \sim 1/(2\tau_c)$, so the icequake frequency we would expect from this cavity collapse is 1.2 Hz. This value is again within the range of peak frequencies observed for calving icequakes at Yahtse Glacier.

[50] Our deceleration model result is consistent with observations from Jakobshavn Isbræ, where the terminus height is approximately 100 m—taller than the 40–80 m termini common at Alaskan Glaciers [Brown *et al.*, 1982; Walter *et al.*, 2012]. At Jakobshavn Isbræ, Amundson *et al.* [2010] report icequakes with emergent onsets, 4–6 Hz dominant frequencies, 5–300 s durations, and associations with rumbling acoustic signals (their “Type 2” seismic signals). The appearance of their example waveform, with higher frequency ground motion early in the icequake arrival, is remarkably similar to the calving icequakes we observe at Yahtse Glacier. Amundson *et al.* [2010] attribute these icequakes to avalanching of debris from the terminus and from icebergs in the fjord rotating and crashing onto dense ice debris mélange. However, the slamming (a) and iceberg deceleration (b) mechanisms are also potential icequake sources in a mélange-choked fjord. As stated above, our model of iceberg deceleration predicts higher frequency seismic signals for larger fall heights. Thus, if some of the type 2 icequakes of Amundson *et al.* [2010] are the product of iceberg calving, iceberg deceleration offers an explanation for why their 4–6 Hz dominant frequencies are slightly higher than the 1–3 Hz frequencies reported at Alaskan glaciers [e.g., O’Neel *et al.*, 2007].

[51] To summarize, both iceberg deceleration (mechanism (b)) and cavity collapse (mechanism (c)) involve forces that act over timescales similar to those we would expect given the observed 1–5 Hz seismic signals described above. This modeling result corroborates the observations reported earlier and increases our confidence that we have identified the correct seismogenic mechanisms. Iceberg slamming (mechanism (a)) and cavity pinch-off (mechanism (d)) can involve forces far greater than those associated with deceleration and cavity collapse, but act over millisecond timescales and, in the case of slamming, may generate a smaller impulse. While we have not explored mechanisms (a) and (d) explicitly, the interaction between brief, high-frequency pressure waves traveling through the water and the surrounding geologic structure may also be compatible with the generation of seismic signals within the 1–5 Hz band identified at Yahtse Glacier and elsewhere.

5.3. Seismic Monitoring of Iceberg Calving

[52] This and previous studies have demonstrated that iceberg calving generates significant seismic energy. However, the use of seismology as a tool to remotely monitor iceberg calving discharge has been hampered by two factors: uncertainty associated with source mechanisms, and the inability to form broadly applicable relationships between iceberg discharge and seismic parameters. We are able to contribute to this development through comparison of calving style and calving seismicity between Yahtse Glacier and nearby Columbia Glacier.

[53] Studies at Columbia Glacier have found no correlation between peak icequake amplitude and the size of calving events [Qamar, 1988; O’Neel *et al.*, 2007]. However, O’Neel *et al.* [2007] successfully used icequake recordings to estimate the rate of terminus retreat at Columbia Glacier. Their approach relied on a calibrated icequake duration metric and an assumption that changes in the rate of terminus retreat are independent of changes in ice velocity. This metric was strongly modulated by relatively infrequent, very large, long-duration (100s s) calving events that involved submarine icebergs discharge.

[54] The importance of calving style on calving seismicity was also manifest at Columbia Glacier during the summer of 2007, when the glacier terminus transitioned from grounded to floating [Walter *et al.*, 2010]. Coincident with that grounded to floating transition was a shift in calving style from frequent, small, energetic calving events (similar to, but bigger than Yahtse Glacier events) to infrequent, larger, less energetic calving events. Calving from the post-2007 floating terminus was characterized by rift propagation leading to the release of tabular icebergs. Accompanying this shift in calving style was a dramatic decrease in the amplitude and occurrence rate of seismic signals between 1 and 5 Hz. Walter *et al.* [2010] found their pre-2007 observations consistent with a hydraulic fracturing source for calving under grounded conditions, in agreement with O’Neel and Pfeffer [2007]. They suggested that when the terminus became afloat, hydraulic fracturing no longer took place at the terminus, altering both the icequake source and the style of calving.

[55] Our result that calved iceberg volume is not proportional to seismic amplitude is consistent with the Columbia Glacier observations [Qamar, 1988; O’Neel *et al.*, 2007]. We observed that iceberg free falls that result in cavitation produce high-amplitude seismograms irrespective of their size. At Yahtse Glacier, simple, 5 s, size 1 calving events produce icequakes detectable at least 13 km from the terminus, and, as demonstrated by the contrasting sizes and peak amplitudes of Block and Flake (Figures 5 and 6), seismic amplitude is not a function of iceberg size. Larger icebergs with short free falls or that detach below the sea surface in the shallow waters of Icy Bay do not move fast enough to form an air cavity in their lee. Forces leading to deceleration will be weaker, and the lack of cavitation results in small peak seismic amplitudes for long event durations.

[56] While hydraulic fracturing might be important in driving some calving events, the present study leads us to favor an alternate explanation for the change in calving seismicity reported at Columbia Glacier in 2007. Consistent with the change in calving style reported by Walter *et al.*

[2010], we suggest that glaciers with floating termini more rarely calve the types of icebergs that cavitate or create large splashes and powerful deceleration forces. Because the thinner, neutrally buoyant post-2007 terminus of Columbia Glacier had less gravitational potential energy, interactions between icebergs and the sea surface were less forceful than from its grounded terminus, and 1–5 Hz calving seismicity is less pronounced.

[57] Our study, and the findings from *Walter et al.* [2010], suggest some caution in the use of 1–5 Hz icequakes for the purpose of studying calving at rapidly changing glaciers with diverse terminus geometries. The generation of icequakes with peak frequencies in this band is substantially dependent on the style of calving, the height of the terminal cliff and the depth of the fjord. For example, if the termini of Yahtse Glacier were to thin, retreat, and eventually switch from grounded to floating, the center of mass of detaching icebergs would approach the waterline (as occurred at Columbia Glacier in 2007). As a result, we would expect that icequake peak frequencies and amplitudes would decrease. Within the limited range of observed terminal cliff heights and iceberg sizes, our numerical model indicates that the peak frequency of calving icequakes should be similar, regardless of whether the calving was subaerial or submarine. Deviations in the peak frequency or seismic amplitude of calving icequakes from a particular tidewater glacier can be expected to indicate a change in terminus geometry and/or calving style, as *Walter et al.* [2010] demonstrated.

[58] With these caveats, future studies that aim to model calving flux from seismic parameters should continue to explore empirical relationships between icequake duration and amplitude as well as other seismic parameters, such as pseudo-energy (integrated squared velocity), coda duration, etc. If statistical modeling is carried out in enough cases and in a diversity of glacierized settings (e.g., thick and thin glaciers, varying levels of ice fracture), then perhaps a general empirical model can be developed that will apply at least to temperate, grounded glaciers. We can expect that a different empirical model would be necessary for floating termini or different calving styles. The development and application of such a model could be a powerful tool for quantifying the mass balance of rapidly changing tidewater glaciers.

6. Conclusions

[59] The seismic wavefield at the terminus of Yahtse Glacier is dominated by icequakes generated by iceberg calving—at least 75% of locally recorded seismic events can be conclusively linked to calving. We observe a strong correlation between calving duration and icequake duration; the relationship between peak icequake amplitude and iceberg size appears to be weak at Yahtse Glacier.

[60] Our paired seismograms and calving videos reveal that interactions between icebergs and the sea surface generate the strongest icequake signals (as illustrated in Figure 1). Seismic energy is produced during iceberg impact on the sea surface as well as several seconds after impact, during cavitation. Cavitation is recognized by the occurrence of Worthington jets, in which water and ice debris are thrown high above the fjord surface. During iceberg impact, when we see steps in the amplitudes of our locally recorded

seismograms, potential seismogenic mechanisms include momentum transfer from icebergs to seawater (Figure 1a) and iceberg deceleration (Figure 1b). Following iceberg impact and coincident with the generation of Worthington jets, we record the largest amplitude portions of each subaerial calving icequake. Air cavity collapse (Figure 1c) and cavity pinch-off (Figure 1d) are the potential seismogenic mechanisms at these times.

[61] Our proposed mechanisms are consistent with the repeated observation that icebergs calved from below the sea surface (submarine calving events) are rarely associated with large amplitude icequakes at Yahtse Glacier. Previous explanations of calving seismicity cannot easily explain the weak submarine calving seismicity described in this study. Compared with observations from deep-water termini [e.g., *Motyka*, 1997], our results suggest that Yahtse Glacier's fjord is too shallow to allow sufficient upward velocity to bring rising submarine icebergs to a height equivalent to the calving face. At glaciers in deeper fjords, submarine calved icebergs have the potential to rise significantly above their neutrally buoyant position (“shooters” in *Motyka* [1997]). When these “shooters” descend, they have the same potential to experience strong drag forces and generate cavities as the subaerially calved icebergs that are most common at Yahtse Glacier.

[62] In a numerical model of iceberg/fjord source mechanisms, we explored the duration of forces associated with both iceberg deceleration and cavity collapse. Both of these mechanisms act over timescales in line with the peak icequake frequencies we document, 1–5 Hz. The other mechanisms considered herein, momentum transfer from iceberg to seawater and cavity pinch-off, act over far shorter timescales and may be associated with smaller impulses. While we cannot discount contributions from other source mechanisms not delineated here, the combination of observations and modeling we have described implicate some iceberg–sea surface interactions as strong sources of tidewater glacier seismicity.

[63] **Acknowledgments.** This study was made possible by the National Science Foundation, through grant EAR-0810313. Additional funding is from USGS Climate and Land Use Change Program and Department of the Interior Climate Science Center. Jeff Aristoff, Channon Price and Wendy Zhang offered insight and enlightening conversation regarding hydrodynamics. Joshua Carmichael, Seth Moran, Victor Tsai, an anonymous reviewer, and our scientific editor, Jeremy Bassis, contributed thorough and constructive reviews. Sophie Gilbert illustrated Figure 1. Justin Rich assisted with the preparation of Figure 2. Expert air support was from pilots Tony Oney and Paul Claus. David Conner and Jared Steyaert assisted with the calving observer record. PASSCAL and UNAVCO provided seismic and geodetic instruments for this work. The Wrangell Mountains Center, McCarthy, AK, provided logistical assistance. The GISMO toolbox significantly facilitated the manipulation and plotting of seismic data [*Reyes and West*, 2011]. We gratefully thank all of the people who contributed to help make this work happen.

References

- Amundson, J. M., M. Truffer, M. P. Lüthi, M. Fahnestock, M. West, and R. J. Motyka (2008), Glacier, fjord, and seismic response to recent large calving events, Jakobshavn Isbræ, Greenland, *Geophys. Res. Lett.*, **35**, L22501, doi:10.1029/2008GL035281.
- Amundson, J. M., M. Fahnestock, M. Truffer, J. Brown, M. P. Lüthi, and R. J. Motyka (2010), Ice mélange dynamics and implications for terminus stability, Jakobshavn Isbræ, Greenland, *J. Geophys. Res.*, **115**, F01005, doi:10.1029/2009JF001405.
- Amundson, J. M., J. F. Clinton, M. Fahnestock, M. Truffer, M. P. Lüthi, and R. J. Motyka (2012), Observing calving-generated ocean waves with

- coastal broadband, Jakobshavn Isbræ, Greenland, *Ann. Glaciol.*, 53(60), 79–84, doi:10.3189/2012/AoG60A200.
- Aristoff, J., T. Truscott, A. Techet, and J. Bush (2010), The water entry of decelerating spheres, *Phys. Fluids*, 22(3), 1–8, doi:10.1063/1.3309454.
- Barclay, D. J., J. L. Barclay, P. E. Calkin, and G. C. Wiles (2006), A Revised and Extended Holocene Glacial History of Icy Bay, Southern Alaska, U.S.A., *Arct. Antarct. Alpine Res.*, 38(2), 153–162, doi:10.1657/1523-0430(2006)38[153:ARAEHG]2.0.CO;2.
- Bassis, J. N., R. Coleman, H. A. Fricker, and J. B. Minster (2005), Episodic propagation of a rift on the Amery Ice Shelf, East Antarctica, *Geophys. Res. Lett.*, 32, L06502, doi:10.1029/2004GL022048.
- Batchelor, G. (1967), *An Introduction to Fluid Dynamics*, 615 pp., Cambridge Univ. Press, Cambridge, U. K.
- Bergmann, R., D. Van Der Meer, S. Gekle, A. Van Der Bos, and D. Lohse (2009), Controlled impact of a disk on a water surface: cavity dynamics, *J. Fluid Mech.*, 633, 381–409, doi:10.1017/S0022112009006983.
- Brown, C. S., M. F. Meier, and A. Post (1982), Calving speed of Alaska tidewater glaciers, with application to Columbia Glacier, *USGS Prof. Pap.*, 1258-C, C1–C13.
- Carmichael, J. D., E. C. Pettit, M. Hoffman, A. Fountain, and B. Hallet (2012), Seismic multiplet response triggered by melt at Blood Falls, Taylor Glacier, Antarctica, *J. Geophys. Res.*, 117, F03004, doi:10.1029/2011JF002221.
- Chouet, B., G. Saccorotti, M. Martini, P. Dawson, G. D. Luca, G. Milana, and R. Scarpa (1997), Source and path effects in the wave fields of tremor and explosions at Stromboli Volcano, Italy, *J. Geophys. Res.*, 102(B7), 15,129–15,150.
- De Backer, G., M. Vantorre, C. Beels, J. De Pré, S. Victor, J. De Rouck, C. Blommaert, and W. Van Paeppegem (2009), Experimental investigation of water impact on axisymmetric bodies, *Appl. Ocean Res.*, 31(3), 143–156, doi:10.1016/j.apor.2009.07.003.
- Deichmann, N., J. Ansoorge, F. Scherbaum, A. Aschwanden, F. Bernardi, and G. H. Gudmundsson (2000), Evidence for deep icequakes in an Alpine glacier, *Ann. Glaciol.*, 31(1), 85–90, doi:10.3189/172756400781820462.
- Ekström, G., M. Nettles, and G. A. Abers (2003), Glacial earthquakes, *Science*, 302(5645), 622–624, doi:10.1126/science.1088057.
- Gaudet, S. (1998), Numerical simulation of circular disks entering the free surface of a fluid, *Phys. Fluids*, 10(10), 2489–2499, doi:10.1063/1.869787.
- Gekle, S., and J. M. Gordillo (2010), Generation and breakup of Worthington jets after cavity collapse. Part 1. Jet formation, *J. Fluid Mech.*, 663, 293–330, doi:10.1017/S0022112010003526.
- Gekle, S., A. van der Bos, R. Bergmann, D. van der Meer, and D. Lohse (2008), Noncontinuous Froude number scaling for the closure depth of a cylindrical cavity, *Phys. Rev. Lett.*, 100(8), 1–4, doi:10.1103/PhysRevLett.100.084502.
- Glasheen, J. W., and T. A. McMahon (1996), Vertical water entry of disks at low Froude numbers, *Phys. Fluids*, 8(8), 2078–2083, doi:10.1063/1.869010.
- Goossens, D. (1987), A drag coefficient equation for natural, irregularly shaped particles, *Catena*, 14(1–3), 73–99, doi:10.1016/S0341-8162(87)80007-3.
- Hotovy, J. D., and N. D. Sylvester (1979), Drag coefficients for irregularly shaped particles, *Indust. Eng. Chem. Proc. Design Dev.*, 18(3), 433–436, doi:10.1021/i260071a014.
- Joughin, I., I. Howat, R. B. Alley, G. Ekstrom, M. Fahnestock, T. Moon, M. Nettles, M. Truffer, and V. Tsai (2008), Ice-front variation and tide-water behavior on Helheim and Kangerdlugssuaq Glaciers, Greenland, *J. Geophys. Res.*, 113, F01004, doi:10.1029/2007JF000837.
- Kanamori, H., and J. W. Given (1983), Lamb pulses observed in nature, *Geophys. Res. Lett.*, 10(5), 373–379.
- Kennett, B. L. N. (2002), *The Seismic Wavefield*, vol. II, *Interpretation of Seismograms on Regional and Global Scales*, 534 pp., Cambridge Univ. Press, Cambridge, U. K.
- Korotkin, A. I. (2009), *Added Masses of Ship Structures*, 401 pp., Springer, Dordrecht, Netherlands.
- May, A., and J. C. Woodhull (1948), Drag coefficients of steel spheres entering water vertically, *J. Appl. Phys.*, 19, 1109–1121.
- Meier, M. F., and A. Post (1987), Fast tidewater glaciers, *J. Geophys. Res.*, 92(B9), 9051–9058.
- Métaxian, J.-P. (2003), Seismicity related to the glacier of Cotopaxi Volcano, Ecuador, *Geophys. Res. Lett.*, 30(9), 1483, doi:10.1029/2002GL016773.
- Miloh, T. (1991), On the initial-stage slamming of a rigid sphere in a vertical water entry, *Appl. Ocean Res.*, 13(1), 43–48.
- Motyka, R. J. (1997), Deep-water calving at LeConte Glacier, southeast Alaska, *Byrd Polar Res. Center Rep.*, 15, 115–118.
- Muskett, R. R., C. S. Lingle, J. M. Sauber, B. T. Rabus, and W. V. Tangborn (2008), Acceleration of surface lowering on the tidewater glaciers of Icy Bay, Alaska, U.S.A. from InSAR DEMs and ICESat altimetry, *Earth Planet. Sci. Lett.*, 265(3–4), 345–359, doi:10.1016/j.epsl.2007.10.012.
- Neave, K. G., and J. C. Savage (1970), Icequakes on the Athabasca Glacier, *J. Geophys. Res.*, 75(8), 1351–1362, doi:10.1029/JB075i008p01351.
- Nettles, M., and G. Ekström (2010), Glacial earthquakes in Greenland and Antarctica, *Ann. Rev. Earth Planet. Sci.*, 38(1), 467–491, doi:10.1146/annurev-earth-040809-152414.
- O’Neel, S., and W. T. Pfeffer (2007), Source mechanics for monochromatic icequakes produced during iceberg calving at Columbia Glacier, AK, *Geophys. Res. Lett.*, 34, L22502, doi:10.1029/2007GL031370.
- O’Neel, S., K. A. Echelmeyer, and R. J. Motyka (2003), Short-term variations in calving of a tidewater glacier: LeConte Glacier, Alaska, U.S.A., *J. Glaciol.*, 49(167), 587–598, doi:10.3189/172756503781830430.
- O’Neel, S., H. Marshall, D. McNamara, and W. T. Pfeffer (2007), Seismic detection and analysis of icequakes at Columbia Glacier, Alaska, *J. Geophys. Res.*, 112, F03S23, doi:10.1029/2006JF000595.
- O’Neel, S., C. F. Larsen, N. Rupert, and R. Hansen (2010), Iceberg calving as a primary source of regional-scale glacier-generated seismicity in the St. Elias Mountains, Alaska, *J. Geophys. Res.*, 115, F04034, doi:10.1029/2009JF001598.
- Porter, S. C. (1989), Late Holocene fluctuations of the fiord glacier system in Icy Bay, Alaska, U.S.A., *Arct. Alpine Res.*, 21(4), 364–379, doi:10.2307/1551646.
- Qamar, A. (1988), Calving icebergs: A source of low-frequency seismic signals from Columbia Glacier, Alaska, *J. Geophys. Res.*, 93(B6), 6615–6623.
- Reyes, C. G., and M. E. West (2011), The waveform suite: A robust platform for manipulating waveforms in MATLAB, *Seismol. Res. Lett.*, 82(1), 104–110, doi:10.1785/gssrl.
- Sabunco, T., and S. Calisal (1981), Hydrodynamic coefficients for vertical circular cylinders at finite depth, *Ocean Eng.*, 8, 25–63.
- Spray, J. G. (1999), Shocking rocks by cavitation and bubble implosion, *Geology*, 27(8), 695–698.
- Stein, S., and M. Wysession (2003), *An Introduction to Seismology, Earthquakes, and Earth Structure*, 498 pp., Blackwell, Malden, Mass.
- St. Lawrence, W., and A. Qamar (1979), Hydraulic transients: a seismic source in volcanoes and glaciers., *Science*, 203(4381), 654–656, doi:10.1126/science.203.4381.654.
- Tsai, V., and G. Ekström (2007), Analysis of glacial earthquakes, *J. Geophys. Res.*, 112, F03S22, doi:10.1029/2006JF000596.
- Tsai, V., J. Rice, and M. Fahnestock (2008), Possible mechanisms for glacial earthquakes, *J. Geophys. Res.*, 113, F03014, doi:10.1029/2007JF000944.
- van der Veen, C. J. (1996), Tidewater calving, *J. Glaciol.*, 42(141), 375–385.
- Walter, F., N. Deichmann, and M. Funk (2008), Basal icequakes during changing subglacial water pressures beneath Gornegletscher, Switzerland, *J. Glaciol.*, 54(186), 511–521, doi:10.3189/00214308785837110.
- Walter, F., J. F. Clinton, N. Deichmann, D. S. Dreger, S. E. Minson, and M. Funk (2009), Moment tensor inversions of icequakes on Gornegletscher, Switzerland, *Bull. Seismol. Soc. Am.*, 99(2A), 852–870, doi:10.1785/0120080110.
- Walter, F., S. O’Neel, D. McNamara, W. T. Pfeffer, J. Bassis, and H. Fricker (2010), Iceberg calving during transition from grounded to floating ice: Columbia Glacier, Alaska, *Geophys. Res. Lett.*, 37, L15501, doi:10.1029/2010GL043201.
- Walter, F., J. M. Amundson, S. O’Neel, M. Truffer, M. Fahnestock, and H. A. Fricker (2012), Analysis of low-frequency seismic signals generated during a multiple-iceberg calving event at Jakobshavn Isbræ, Greenland, *J. Geophys. Res.*, 117, F01036, doi:10.1029/2011JF002132.
- Welty, E., T. C. Bartholomäus, S. O’Neel, and W. T. Pfeffer (2012), Cameras as clocks, *J. Glaciol.*, doi:10.3189/2013JoG12J126, in press.
- West, M., C. Larsen, M. Truffer, S. O’Neel, and L. LeBlanc (2010), Glacier microseismicity, *Geology*, 38(4), 319–322, doi:10.1130/G30606.1.
- Whipple, K. X., G. S. Hancock, and R. S. Anderson (2000), River incision into bedrock: Mechanics and relative efficacy of plucking, abrasion, and cavitation, *Geol. Soc. Am. Bull.*, 112(3), 490–503.
- Wiens, D. A., S. Anandakrishnan, J. P. Winberry, and M. A. King (2008), Simultaneous teleseismic and geodetic observations of the stick-slip motion of an Antarctic ice stream., *Nature*, 453(7196), 770–774, doi:10.1038/nature06990.
- Winberry, J. P., S. Anandakrishnan, and R. B. Alley (2009), Seismic observations of transient subglacial water-flow beneath MacAyeal Ice Stream, West Antarctica, *Geophys. Res. Lett.*, 36, L11502, doi:10.1029/2009GL037730.
- Winberry, J. P., S. Anandakrishnan, D. A. Wiens, R. B. Alley, and K. Christianson (2011), Dynamics of stick-slip motion, Whillans Ice Stream, Antarctica, *Earth Planet. Sci. Lett.*, 305(3–4), 283–289, doi:10.1016/j.epsl.2011.02.052.
- Wolf, L. W., and J. N. Davies (1986), Glacier-generated earthquakes from Prince William Sound, Alaska, *Bull. Seismol. Soc. Am.*, 76(2), 367–379.